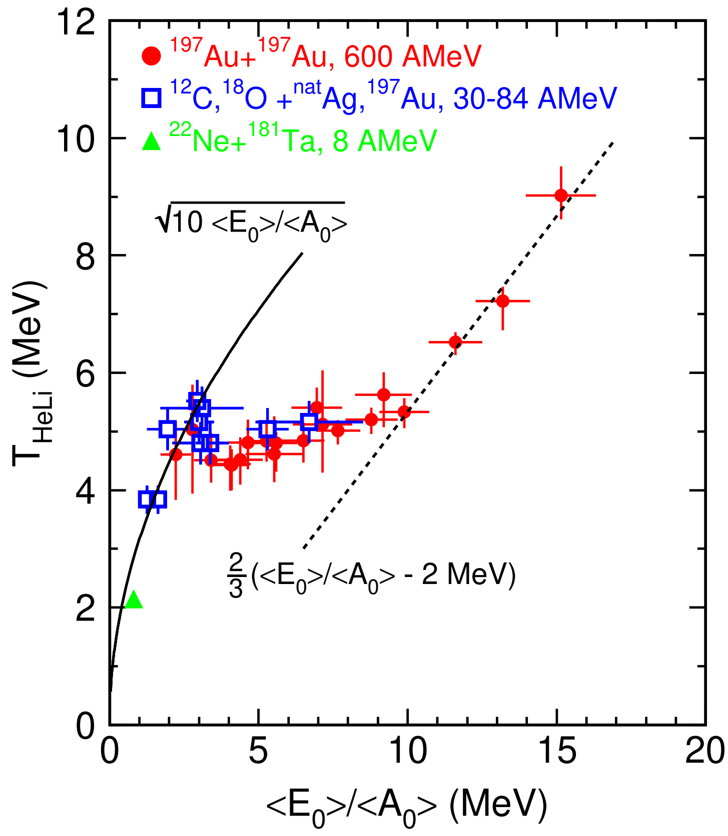

Caloric curve of nuclei determined by the dependence of the temperature T_{HeLi} - derived from observed yield ratios of He and Li isotopes - on the excitation energy per nucleon. The rise of T_{HeLi} for excitation energies below 2 MeV per nucleon is compatible with an evaporative decay of a Fermi liquid (solid line). Beyond a total excitation energy of 10 MeV per nucleon, the steady increase of T_{HeLi} with increasing $\langle E_0\rangle/\langle A_0\rangle$ with a slope of 2/3 (dashed line) alludes to a gas of classical, elementary particles. The plateau of the caloric curve joining the liquid-like and the gas-like regions is suggestive of a first-order phase transition with a substantial latent heat and is reminiscent of the paradigm of a phase transition, the first-order phase transition of water. However, for such a finite system, the shape of the caloric curve is also consistent with a transition in close proximity to the critical point, which is the *sine qua non* for the determination of critical-point properties.

Boiling Nuclei

New results from the analysis of ALADIN data for the fragmentation of heavy projectiles at relativistic bombarding energies are reported. Evidence for a high degree of equilibration of the excited projectile spectators is found in the Z_{bound} universality of their decay patterns. The mass and the deposited excitation energy of the spectator prior to its decay are determined from balance equations. The experimental input to these equations includes the multiplicities and kinetic energies of free neutrons measured in coincidence with LAND. The temperatures at breakup are determined from isotopic yields of light fragments. The caloric curve of nuclei, obtained by plotting the temperature T versus the excitation energy E/A, is characterized by a plateau of $T \approx 5$ MeV up to $E/A \approx 10$ MeV and a rise of T at higher excitation. In an attempt to deduce critical parameters of the nuclear liquid-gas phase transition, the role of finite size effects is studied.

1 Introduction

Heavy-ion reactions at relativistic bombarding energies offer a wide range of possibilities for studying multi-fragment decays of highly excited atomic nuclei. The largest fragment multiplicities measured so far were observed in central ^{197}Au on ^{197}Au collisions at a bombarding energy of 100 MeV per nucleon [1]. In these collisions the system of nearly 400 nucleons disintegrates completely into nuclear fragments and light particles. The analysis of the kinetic energy spectra in these reactions has revealed a considerable collective outward motion superimposed on the random motion of the constituents at the breakup stage (radial flow) which represents up to one-half of the incident kinetic energy in the center-of-mass frame [2]. This feature prevails, with monotonously increasing flow values, over the range of bombarding energies up to 1000 MeV per nucleon [3]. It demonstrates the strong dynamical coupling between entrance and exit channels in central collisions of heavy systems.

The process of fragment formation is found to be sensitive to the flow dynamics. The measured relative element yields are systematically correlated with the magnitude of the observed radial flow [3, 4]. Within a coalescence picture, the suppression of heavier fragments for larger flow values may be caused by the reduction of the density in momentum space associated with the collective expansion [4]. The interplay of dynamical and statistical effects in these violent collisions is currently a matter of high interest [5].

Multi-fragment decays are also observed in more peripheral nucleus-nucleus collisions at high energies. The spectator systems formed during the initial stages of the reaction may be excited to an extent that complete breakups can occur. Here, in contrast to central collisions, no apparent dependence on the entrance channel is observed. The decay patterns were found to be mainly governed by the energy transfer to the spectator, as evident from the Z_{bound} scaling of the fragment charges and their correlations [6, 7]. The quantity Z_{bound} is defined as the sum of the charges of all product nuclei with $Z \geq 2$ and is related to the energy deposit. When plotted as a function of this quantity the fragment multiplicities and correlations exhibit a universal behaviour. It was first observed as an invariance with respect to the chosen target in the decays of ^{197}Au projectiles at 600 MeV per nucleon [6, 8].

In this report we will concentrate on the latter type of multifragmentation. Its invariant

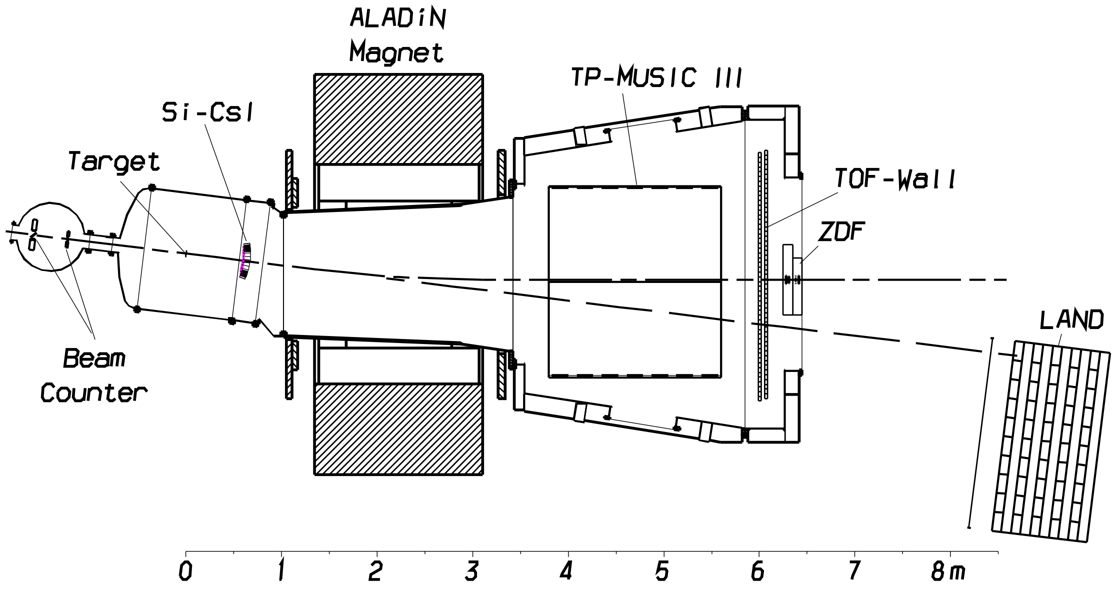

Figure 1: Cross-sectional view of the ALADIN facility. The beam enters from the left and is monitored by the beam counters before reaching the target. The entrance to the dipol magnet is surrounded by the Si-CsI(Tl) array. Projectile fragments are tracked and identified in the TP-MUSIC III detector and in the time-of-flight wall. Coincident neutrons emitted approximately in the direction of the incident beam (dashed line) are detected with the large-area neutron detector (LAND). The dash-dotted line represents the trajectory of beam particles after they were deflected by an angle of 8°.

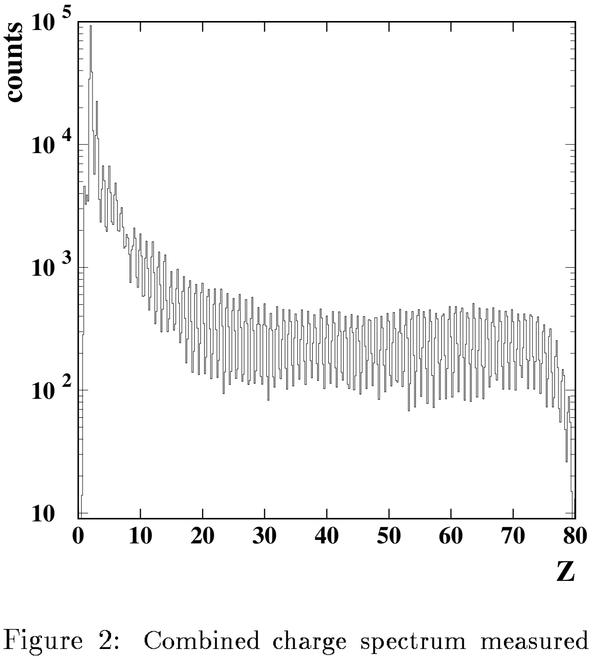

Figure 2: Combined charge spectrum measured with the TP-MUSIC detector and the TOF-Wall of the ALADIN forward spectrometer system for reactions with ^{197}Au projectiles.

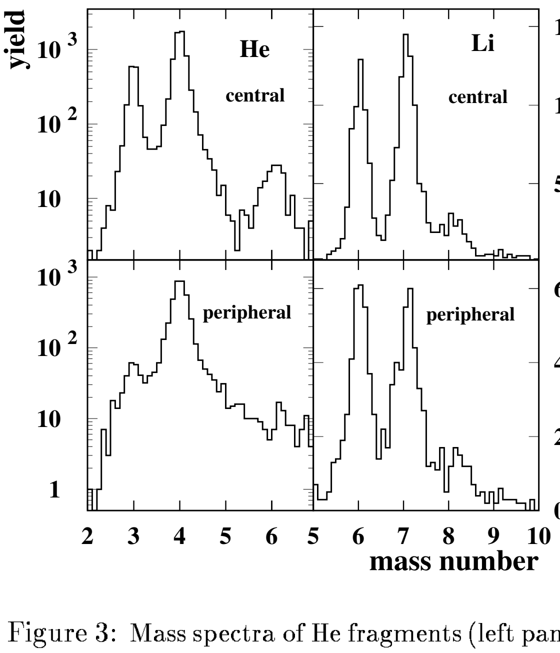

Figure 3: Mass spectra of He fragments (left panel) and Li fragments (right panel). The upper parts display central collisions while the lower parts show the distributions for peripheral collisions.

features are consistent with equilibration of the excited systems prior to their decay. Equilibration, on the other hand, will facilitate interpretations in statistical or thermodynamical terms. Multifragmentation has been considered a manifestation of the liquid-gas phase transition in finite systems. The pursuit of this challenging question will profit from the study of equilibrated systems that may be characterized by a few global variables such as mass, excitation energy, or temperature. Clearly, the aim must be to determine these quantities experimentally. The present status of our efforts in this direction is summarized in this report.

2 Experimental Setup

The experimental setup (Fig. 1) resembles that used in earlier experiments but was modified in several respects: The solid angle adjacent to the acceptance of the ALADIN magnet was covered by the Catania hodoscope which consists of 84 Si-CsI(Tl) telescopes in closely packed geometry and which extends to angles up to $\Theta_{lab} \approx 16°$. The TP-MUSIC III served as the tracking detector. The multiple sampling of the ionization charges resulted in a resolution of ΔZ = 0.4 (FWHM) for fragments with atomic number $Z \geq 8$. Lighter fragments were tracked and identified by collecting and amplifying their ionization charges with proportional counters mounted in three positions at the anode plane of the drift volume. The two-layered time-of-flight wall extended over a horizontal range of 2.4 m. The primary beam and projectile fragments emitted along directions close to that of the beam were detected with a plastic detector with light-fiber readout (denoted ZDF in Fig. 1). The large-area neutron detector LAND [9] was positioned close to zero degrees with respect to the incident beam direction and operated in a calorimetric mode.

The charge identification capability of the ALADIN setup is illustrated in Fig. 2. Complete tracking information was obtained for 32% (70%) of all detected Z=2 (Z=10) particles. By combining this information with the time-of-flight measurement, the masses of light fragments were determined with a resolution of about ΔA_{FWHM}=0.3 (0.5) for Z=2 (Z=10) particles, respectively (Fig. 3).

3 Dependence on Projectile Energy and Mass

The ALADIN spectrometer has been designed for optimum acceptance of projectile fragments which are focussed in forward directions. The focussing effect, however, is a function of the projectile velocity and changes with changing bombarding energy.

We have therefore studied the extension of the projectile-spectator source in rapidity y and transverse momentum p_t both with experimental data and with model calculations. Guided by these analyses we define the spectator source in rapidity by the condition $y \geq 0.75 \cdot y_{proj}$, where y_{proj} is the projectile rapidity, and by upper limits in the laboratory angle. The angular cuts were chosen inversely proportional to the projectile momentum. This was motivated by the observation that the widths of the transverse momentum distributions are independent of the bombarding energy. At the lower bombarding energies these angular cuts include some of the detectors of the Si-CsI(Tl) telescope array.

In Fig. 4 the mean number of intermediate-mass fragments (IMF's, $3 \leq Z \leq 30$) is shown as a function of Z_{bound} for the reaction of ^{197}Au on ^{197}Au at four bombarding energies. With the definition of the projectile spectator given above the correlation between the two quantities is seen to be independent of the projectile energy within the experimental accuracy. The maximum mean multiplicity of 4 to 4.5 fragments is reached at $Z_{bound} \approx 40$.

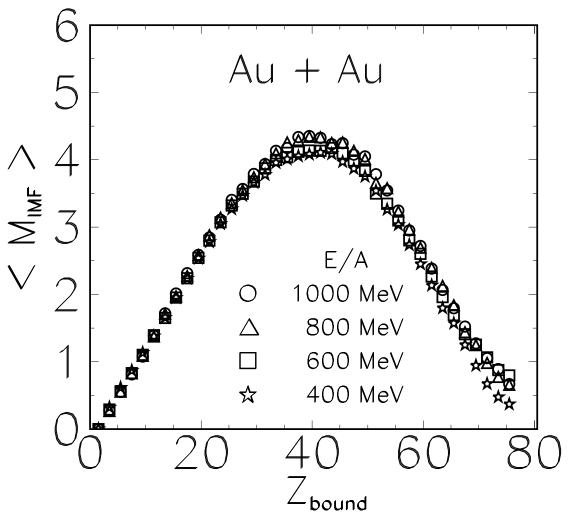

Figure 4: Mean IMF multiplicity $\langle M_{IMF} \rangle$ as a function of Z_{bound} for the reaction of ^{197}Au on ^{197}Au at E/A = 400, 600, 800, and 1000 MeV.

The M_{IMF} versus Z_{bound} correlation depends on the mass of the projectile (Fig. 5, left-hand-side). More fragments are to be expected from heavier projectiles. However, this relation turns out to be almost perfectly proportional to the projectile mass viz. charge (Fig. 5, right-hand-side). For this comparison the upper limit of the IMF definition was changed from $Z \leq 30$ to $Z \leq Z_{proj}/3$. Since the element yields decrease rapidly with Z the upper limit is not crucial. The observed invariance with respect to the entrance channel is not restricted to the multiplicity of intermediate-mass fragments but appears to be a very general feature also of the relative asymmetries and other correlations between the abundancies and the atomic numbers of the fragmentation products [7].

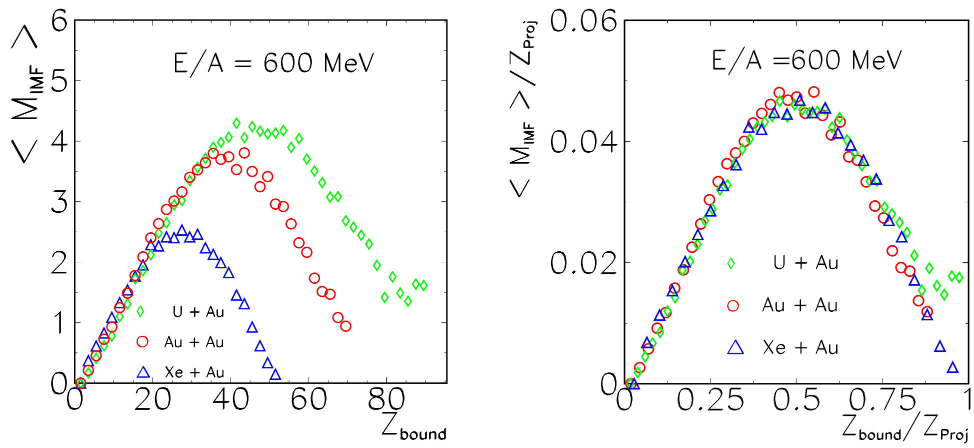

Figure 5: Correlation between the mean multiplicity of intermediate-mass fragments $\langle M_{imf} \rangle$ and Z_{bound} for the reactions ^{238}U on ^{197}Au (diamonds), ^{197}Au on ^{197}Au (circles), and ^{129}Xe on ^{197}Au (triangles) at $E/A = 600$ MeV, as measured with the TOF-wall (left). The same correlation but normalized with respect to the projectile atomic number Z_{proj} (right).

4 Limits of the Universality of Spectator Decay

The observed universality gives rise to the question as to where its limits may lie. Our data for collisions with rather light targets such as beryllium or carbon indicate that, in these cases, beam energies considerably above 400 MeV per nucleon are required in order to reach the maximum IMF production. This is illustrated in Fig. 6 where the fragment multiplicities are plotted as

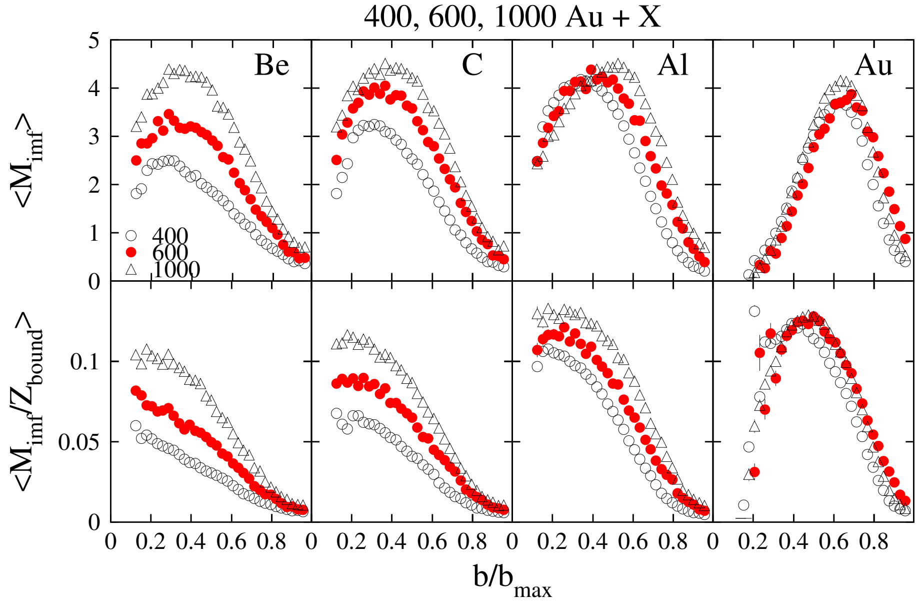

Figure 6: Mean multiplicity of intermediate-mass fragments $\langle M_{imf} \rangle$ (top) and normalized multiplicity $\langle M_{imf}/Z_{bound} \rangle$ (bottom) as a function of the deduced relative impact parameter b/b_{max} for the reactions of ^{197}Au projectiles with Be, C, Al, and Au targets at bombarding energies of 400, 600, and 1000 MeV per nucleon.

a function of the relative impact parameter b/b_{max}. The impact parameter b was deduced by assuming a monotonous relation between b and Z_{bound}. The data for the Au target exhibit energy independent maxima consistent with the invariance discussed in the last section. At 1000 MeV per nucleon, the maximum shifts to smaller impact parameters with decreasing target mass but always assumes the same value, again consistent with the Z_{bound} universality. At 400 MeV per nucleon, in contrast, the maxima of the multiplicity distributions are considerably reduced already for the carbon target.

The lower part of Fig. 6 shows the normalized multiplicities $\langle M_{IMF}/Z_{bound} \rangle$. In first order, they are independent of the size of the decaying system and may thus reflect the relative degree of spectator excitation. The data for the beryllium target, in particular, illustrate that, at energies below 1000 MeV per nucleon, the spectators formed even in the most central collisions are not sufficiently excited in order to undergo a complete breakup.

On the high-energy side, there is no limit known at present. Limiting fragmentation, i.e. a saturation of the production cross sections for intermediate mass fragments at bombarding energies in excess of several GeV, has been observed [10]. It suggests that the formation of spectator nuclei with high excitation energies may be common to heavy-ion collisions in the GeV range. A recent study performed with ^{197}Au beams of 10.6 GeV per nucleon, available from the AGS at Brookhaven, and emulsion targets [11] reports nearly quantitative agreement with the fragmentation patterns of ^{197}Au on Cu collisions at 600 MeV per nucleon [6].

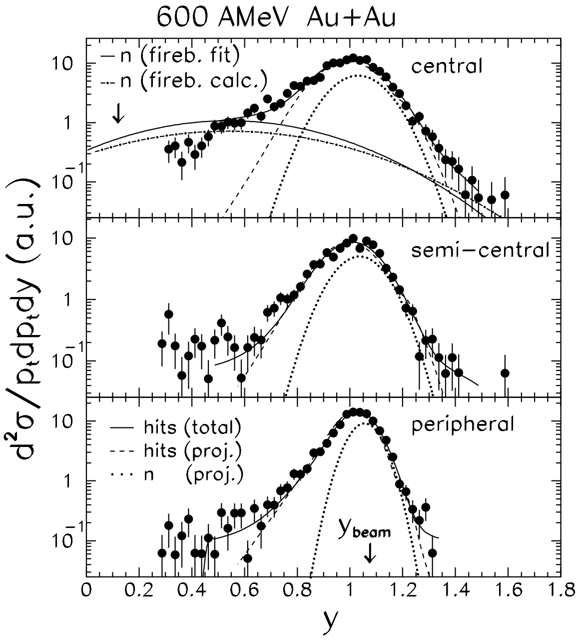

Figure 7: Rapidity distributions of neutron hits in LAND for the transverse momentum bin 20 MeV/c $\leq p_t \leq$ 25 MeV/c (points). The dotted lines represent the fit results for neutrons emitted by the projectile-spectator source. The contribution from the mid-rapidity source is shown for central collisions (top panel).

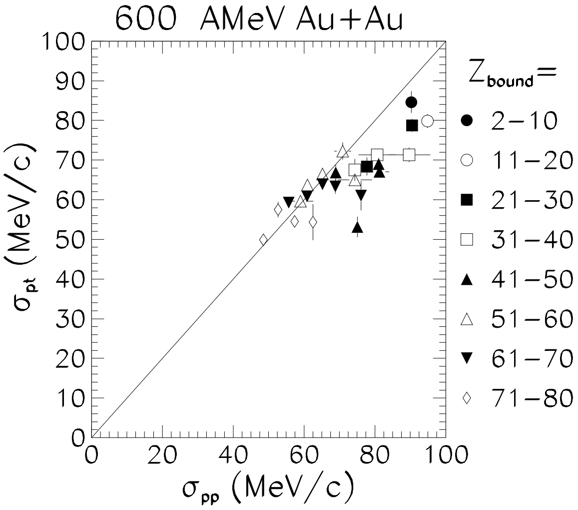

Figure 8: Transverse versus parallel widths of the neutron-momentum distributions for 10-unit wide bins in Z_{bound} and Z_{max} (not indicated) for the reaction of ^{197}Au on ^{197}Au at $E/A = 600$ MeV.

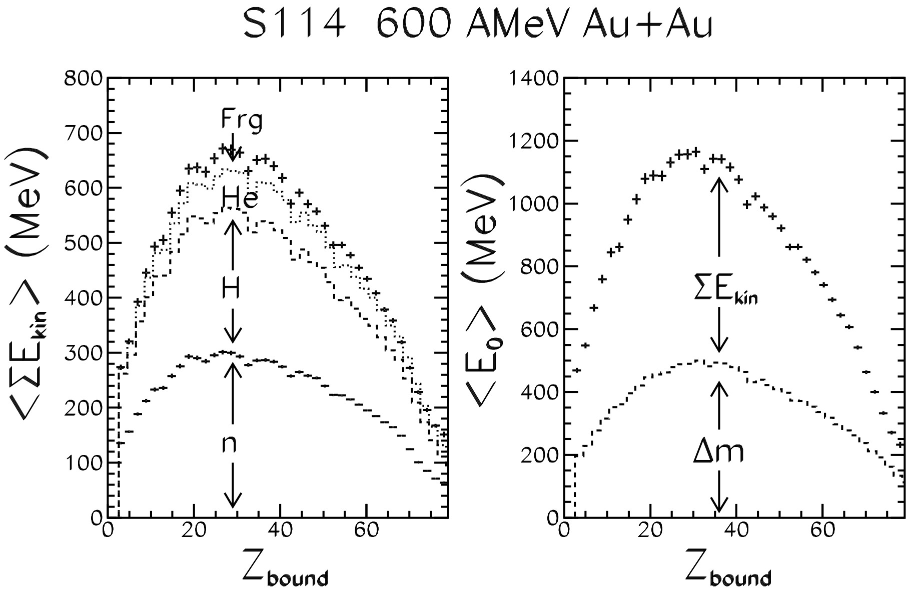

Figure 9: Individual contributions to the total kinetic energy (left-hand-side) and contributions by the total Q-value Δm and by the sum of the kinetic energies to the total energy of the spectator (right-hand-side).

5 Neutrons from Spectator Decays

Neutrons from the decay of the excited spectator sources were detected with the large-area neutron detector LAND which was positioned close to zero degrees at about 9 m downstream from the target. The thickness of 1 m of the calorimeter-type detector permits the detection of fast neutrons with high efficiency (e.g., 94% for 600-MeV neutrons).

Fig. 7 shows the rapidity distribution of neutron hits in LAND for central, semi-central, and peripheral collisions. The distributions are well described by a sum of two gaussian distributions, folded with the detector response (full line). The detector response was determined by using monoenergetic neutrons from deuteron break-up. The two gaussian distributions represent neutron emission from the fireball and from the projectile spectator or its fragments. The spectator source of neutrons moves with a rapidity very close to the beam rapidity of $y_{beam} = 1.07$ (after traversing one-half of the target).

The widths of the transverse distributions of neutron momenta have been determined from fits to the observed parts of the distributions within the covered range of neutron transverse momenta (Fig. 8). The widths increase for the bins of smaller Z_{bound} which indicates a larger temperature of the emitting source in the most central collisions. Figure 8, in particular, shows that the perpendicular and transverse widths are nearly identical. The neutron momentum distributions thus support the idea of equilibration at an early reaction stage.

6 Excitation Energy prior to Fragment Decay

The procedure used to determine the mass and excitation energy prior to the spectator decay is very similar to that proposed by Campi et al. [12]. However, besides the multiplicities and energies of charged particles and fragments also those of free neutrons were included in the analysis.

The basic idea is to determine the atomic number Z_0, the mass number A_0, and the excitation energy E_0 of the excited spectator from balance equations. Since the hydrogen isotopes were not detected assumptions concerning the overall N/Z ratio of the spectator, the intensity ratio of protons, deuterons, and tritons, and the kinetic energies of hydrogen isotopes had to be made. In addition, the EPAX parameterization [13, 14] was used for deriving masses from the atomic numbers of the detected fragments. The uncertainties resulting from the variation of these quantities within reasonable limits are included in the adopted errors.

It is found that light particles and, in particular, the neutrons contribute considerably to the energy balance (Fig. 9). Independent of Z_{bound}, the Q value amounts to about 40% of the total spectator energy E_0.

The results for the mass A_0 and for the specific excitation energy E_0/A_0 are given in Fig. 10. The data points represent the results for individual bins in the Z_{max}-versus-Z_{bound} event representation. The mass A_0 decreases with decreasing Z_{bound} but, apparently, independent of Z_{max}. The smallest mean spectator mass in the bin of $Z_{bound} \leq 10$ is $\langle A_0 \rangle \approx 50$. The excitation energy E_0 appears to be a function of both Z_{bound} and Z_{max}; the higher values correspond to the smaller Z_{max} values, i.e. to more complete disintegrations of a system of given mass. The maximum number of fragments, observed at $Z_{bound} \approx 40$, is associated with initial excitation energies of $\langle E_0 \rangle / \langle A_0 \rangle \approx 8$ MeV. With decreasing Z_{bound} the deduced excitation energies reach up to $\langle E_0 \rangle / \langle A_0 \rangle \approx 15$ MeV. These energy deposits for the range of small Z_{bound} are considerably larger than those obtained from the statistical analysis of the charge correlations of intermediate mass fragments ($Z \geq 3$) for ^{197}Au + Cu collisions at 600 MeV per nucleon [14].

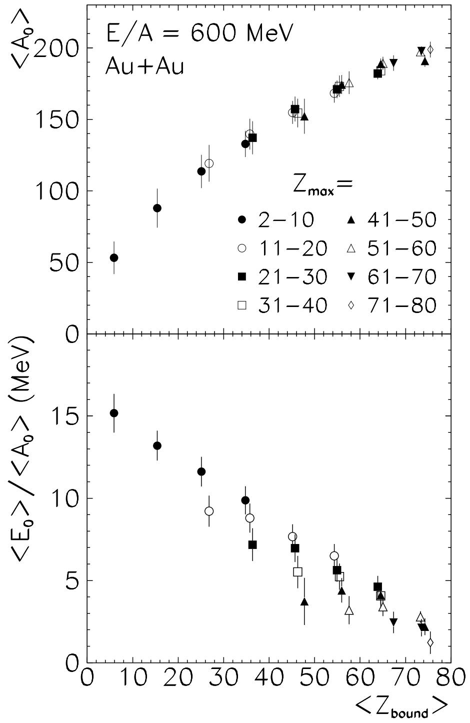

Figure 10: Mass $\langle A_0 \rangle$ (top) and specific excitation energy $\langle E_0 \rangle / \langle A_0 \rangle$ (bottom) of the spectator as a function of Z_{max} and Z_{bound} for the reaction of ^{197}Au on ^{197}Au at $E/A = 600$ MeV.

7 The Quest for the Liquid-Gas Phase Transition

Stimulated by the van der Waals behavior of the nucleon-nucleon force [15-17] and supported by the observation of a power law for the produced fragments in proton induced collisions [18], the idea of a liquid-gas phase transition in nuclear matter emerged [15,16,19-21] and even speculations on a second order phase transition at the critical point [22] were raised [23, 24]. In the subsequent years, interest in this phenomenon faded once the universality - and the corresponding 'theory-invariance' - of the observed power law and the associated critical-point exponent τ emerged (see e.g. refs. [25, 26]). In the meantime, renewed interest arouse just because of the similarities between very different phenomena [27] and - most recently - because of the attempt to extract critical-point exponents of fragmenting nuclear systems produced in the interaction of 1 AGeV Au nuclei with a carbon target [28, 29].

Searching for signals of a nuclear phase transition, we are confronted with at least four complications which are inherent – albeit not specific – for nuclear systems:

(1) Nuclei are composed of a limited number of constituents. For finite systems a broadening of a phase transition [30, 31] and a reduction of the critical temperature from its bulk value of 15-20 MeV is expected [16,31-34].

(2) Nuclei are charged. The long-range Coulomb-repulsion between the constituent protons introduces instabilities [35] which may lead to a considerable shift of the critical temperature downwards to values around 5 MeV [17, 36, 37].

(3) Nuclei are transient systems without external field (e.g. pressure) and will, therefore, expand

prior to their disassembly [21,38-42]. Furthermore, the aggregation into clusters gives rise to an effective equation-of-state [43].

(4) Nuclei are closed systems without a heat bath. Consequently, the temperature of the system cannot be pre-determined but has to be reconstructed from observable quantities.

Generally, phase transitions of rather small clusters ($\sim$10 constituents) are still well defined, distinguishable [31,44-46] and even detectable [47]. Excited nuclei, however, are generated in energetic nucleus-nucleus collisions whose complex dynamical evolution may obscure or even destroy possible signals of a phase-transition. As discussed in more detail in the previous sections, spectator matter seems to be ideally suited to investigate a thermally-driven phase transition: As indicated by the universality of the projectile fragment distributions discussed in section 3, the memory of the entrance channel dynamics is lost prior to the decay of the spectators and the radial flow dynamics, which was shown to affect the fragmentation process [4], is small in these systems [4, 48].

8 The Isotope Thermometer

For a microcanonical ensemble, the thermodynamic temperature T of a system with total energy E may be defined in terms of the total-energy state density $\Omega(E)$ via the relation

$$\frac{1}{T(E)} = \frac{\partial\,(ln\Omega(E))}{\partial E}.$$

An experimental determination of the state density $\Omega(E)$ and its energy dependence is, however, hitherto impossible. Therefore, nuclear temperature determinations take recourse to 'simple' observables which constitute - at least for some ideal situations and generally within a canonical treatment - a good approximation to the true thermodynamic temperature. For example, for a nuclear system at low density and in chemical and thermal equilibrium a measure of the temperature T of the system may be obtained via double ratios of two isotope pairs (Y_1/Y_2) and (Y_3/Y_4) differing by the same number of neutrons and/or protons [49]:

$$R = \frac{Y_1/Y_2}{Y_3/Y_4} = a \cdot e^{[(B_1-B_2)-(B_3-B_4)]/T}. \qquad (1)$$

Here, B_i denotes the binding energy of particle species i and the constant a contains known spins and mass numbers of the fragments. Of course, a meaningful temperature scale can only be derived if the ratio R is sufficiently sensitive to the temperature of the system and if the yields of the considered fragments are measurable over a large range of excitation energy. A large sensitivity of this thermometer may be achieved if the constant $b = (B_1 - B_2) - (B_3 - B_4)$ is larger than the typical temperature to be measured. In table 1 numerical values for the parameters a and b are listed for several isotope pairs. Particularly large values for b are obtained if a $^3He/^4He$ ratio is involved. Indeed, the large cross section of He fragments as an abundant constituent in both the 'liquid' and the 'vapor' regime of nuclear systems *and* the strong binding energy of the α-particle is the lucky coincidence which is the basis of the temperature determination presented hereafter. In order to acquire also for the second yield ratio a sufficient production yield we define in the following a temperature $T_{HeLi,0}$ in terms of the yield ratios ^{3}He/^{4}He and ^{6}Li/^{7}Li

$$T_{HeLi,0} := 13.33/ln(2.18 \cdot \frac{Y_{6Li}/Y_{7Li}}{Y_{3He}/Y_{4He}}). \qquad (2)$$

1. ratio	2. ratio	a	b
$^3He/^4He$	$^6Li/^7Li$	2.18	13.33
	$^7Li/^8Li$	1.98	18.54
	$^9Be/^{10}Be$	0.38	13.77
	$^{10}B/^{11}B$	0.86	9.12
	$^{11}B/^{12}B$	1.11	17.21
$^6Li/^7Li$	$^7Li/^8Li$	0.91	5.22
	$^9Be/^{10}Be$	0.17	0.44
	$^{10}B/^{11}B$	0.39	-4.21
	$^{11}B/^{12}B$	0.51	3.88
$^7Li/^8Li$	$^9Be/^{10}Be$	0.19	-4.78
	$^{10}B/^{11}B$	0.43	-9.42
	$^{11}B/^{12}B$	0.56	-1.34
$^9Be/^{10}Be$	$^{10}B/^{11}B$	2.25	-4.64
	$^{11}B/^{12}B$	2.92	3.44
$^{10}B/^{11}B$	$^{11}B/^{12}B$	1.30	8.09

Table 1: Constants a and b entering into Eq. (1) for different combinations of isotope pairs.

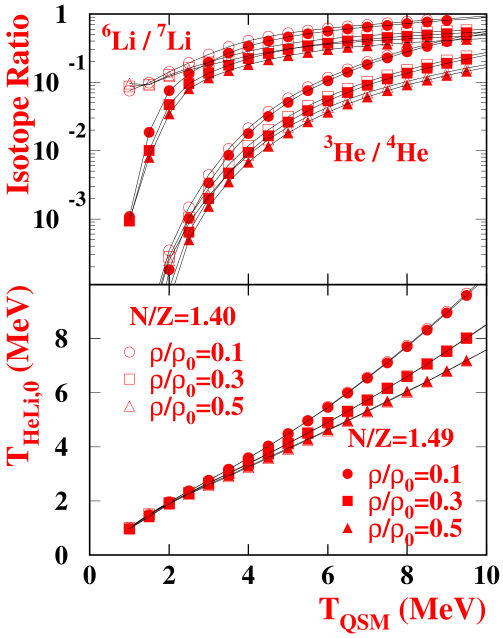

Figure 11: Single isotope ratios (top part) and $T_{HeLi,0}$ (bottom part) calculated from the fragment distribution of the QSM model [50, 51] as a function of the initial temperature.

Up to this point we considered nuclei in their ground state only and we ignored the effect of sequential decays during the final stage of the disassembly process. In particular, the yield of α-particles may be modified by secondary decays. (Note, however, that the effect of the α-feeding is partially neutralized by the feeding of ^3He.) Differentiating Eq. (1), the relative variation of the temperature for a relative change of the double ratio R can be written as

$$\frac{\Delta T}{T} = -\frac{T}{b}\frac{\Delta R}{R}.$$

Assuming a typical temperature of 5 MeV, a modification of R by ±50% causes a change of the extracted temperature $T_{HeLi,0}$ by only ∓19% or ΔT=∓1.0 MeV.

9 Calibration of the Temperature Scale

In order to test the model dependence of the temperature definition via Eq. (2) and to investigate the influence of sequential decays we analyzed the fragment distributions predicted by several decay models.

Isotope ratios of $^6Li/^7Li$ and $^3He/^4He$ calculated by the quantum statistical model (QSM) [50, 51] are shown in the upper part of Fig. 11 as a function of the initial temperature T_{QSM}. Both, the breakup density ρ/ρ_0 and the N/Z ratio of the initial system, influence the individual isotope ratios. Evaluating, however, the double-ratio (or $T_{HeLi,0}$) the influence of the N/Z ratio of the emitting system cancels nearly completely and the uncertainty of T_{QSM} due to variations of the breakup density is reduced by roughly a factor of two as compared to the case where the temperature would have been determined e.g. from the $^3He/^4He$ ratio alone (lower part of Fig. 11).

Despite the strong feeding of the light particle yields through secondary decays the QSM calculations predict an almost linear dependence of $T_{HeLi,0}$ on the actual temperature T of the system. For temperatures below 10 MeV, the ratio $T_{HeLi,0}$/T varies between about 0.95$\pm$0.05 and 0.75$\pm$0.05 for breakup densities between 0.1$\cdot\rho_0$ and 0.5$\cdot\rho_0$.

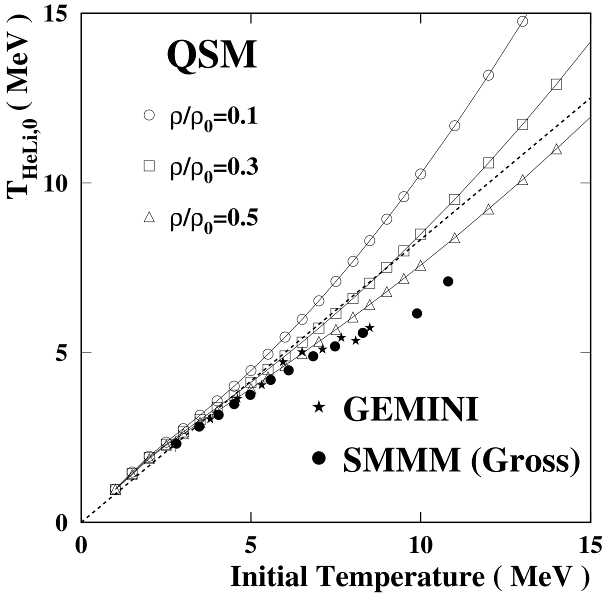

Figure 12: T_{HeLi} calculated from fragment distributions of different decay models as a function of the initial temperature.

Results of sequential evaporation calculations with the code GEMINI [52] also confirm a nearly linear relation between $T_{HeLi,0}$ and the *initial* temperature of the system $T = \sqrt{k \cdot \langle E_0 \rangle / \langle A_0 \rangle}$, where k denotes the inverse level density parameter (see stars in Fig. 12). In line with QSM calculations for higher densities the ratio $T_{HeLi,0}/T \approx 0.7$. Finally, also the microcanonical multifragmentation model of Gross and co-workers [37] predicts a rather constant ratio of 0.7 $\pm$0.05 between $T_{HeLi,0}$ and the thermodynamic temperature of the system (solid dots in Fig. 12).

In order to account pragmatically for the systematic underestimation of the temperature by the quantity $T_{HeLi,0}$, we define the final isotope temperature via

$$T_{HeLi} = 1.2 \cdot T_{HeLi,0}.$$

Thus, T_{HeLi} provides - within the models mentioned and within $\pm$15% - a common temperature scale in the evaporation, the fragmentation as well as in the vapor regime of nuclear systems.

10 The Caloric Curve of Nuclei

The cover figure shows the isotope temperature as a function of the total excitation energy per nucleon which was determined as described in section 6. It is important to note, that the isotope temperature and the excitation energy are practically independent observables, thus avoiding auto-correlations when plotted against each other.

Excitation energy - temperature pairs of this caloric curve extracted for projectile spectators of Au+Au collisions at E/A=600 MeV are marked by the solid points. Data for target residues produced at intermediate energies between E/A=30 and 84 MeV are shown by the open squares. In the latter case, the excitation energies were also deduced from an energy balance [53] and T_{HeLi} was evaluated using the coincident light particle yields associated with emission from the target remnant [54]. Because of the finite width of the excitation energy distribution and the exponentially decreasing production rate of ^{3}He towards low excitation energies temperatures can not be determined for excitation energies below approximately 2 MeV per nucleon in the present study. The only value for T_{HeLi} in the evaporation regime below 2 MeV per nucleon excitation energy is provided by the ^{22}Ne+^{181}Ta fusion reactions at E/A=8.1 MeV [55] and is marked by the triangle in the cover figure.

The obtained caloric curve can be divided into three distinctly different sections. In line with previous studies in the fusion evaporation regime [56, 57] the rise of T_{HeLi} for excitation energies below 2 MeV per nucleon is compatible with the low-temperature approximation of a fermionic system

$$T = \sqrt{k \cdot \langle E_0 \rangle / \langle A_0 \rangle}. \tag{3}$$

For orientation, the solid line depicts relation (3) for an inverse level density parameter of k=10 MeV. Within the range of $\langle E_0 \rangle / \langle A_0 \rangle$ from 3 MeV to 10 MeV an almost constant value for T_{HeLi} of about 4.5-5 MeV is observed. This plateau may be related to the finding of rather constant emission temperatures over a broad range of incident energies which were deduced from the population of particle unstable levels in He and Li fragments [58]. We also note that the mean excitation energy of the plateau coincides with the limiting excitation energy for the fusion-evaporation process of about 4.5-6.4 MeV per nucleon [59]. Finally, beyond a total excitation energy of 10 MeV per nucleon, a steady rise of T_{HeLi} with increasing $\langle E_0 \rangle / \langle A_0 \rangle$ is seen which may be described by a linear relation

$$T_{HeLi} = 2/3 \cdot (\langle E_0 \rangle / \langle A_0 \rangle - 2MeV) \tag{4}$$

where the slope of 2/3 alludes to a gas of classical, elementary particles.

The offset in Eq. (4) probably signals a freeze out at a finite density. Assuming, for simplicity, a parabolic shape for the low density equation-of-state of the finite nuclear system [60]

$$(E/A)_{T=0} = K_c/18 \cdot (1 - \rho/\rho_0)^2 - 8MeV$$

and adding the excitation energy for a Fermi-Dirac gas at finite density, the data in the vapor regime at $\langle E_0 \rangle / \langle A_0 \rangle > 10$ MeV can be explained with a constant freeze-out density between ρ/ρ_0=0.15 and 0.3 if the compressibility K_c is varied between 144 and 300 MeV. While this interplay between the expansion dynamics and the density dependent properties of a Fermi gas might help to elucidate the gross features of the vapor branch, one has to keep in mind that also in this regime typically 20% of the mass of the decaying system is contained in intermediate mass fragments. An internally consistent equation-of-state taking into account the formation of clusters [43], the particle loss during the expansion [40, 42] and the systematic variation of the source size is therefore required before more definite conclusions can be drawn.

The plateau of the caloric curve is suggestive of a first-order phase transition with a substantial latent heat. It also seems to exclude - on first sight - the occurence of a second-order phase transition which is the *sine qua non* for the determination of critical-point exponents [28, 29]. For a finite system with N constituents a transition is, on the other hand, no longer characterized by a singular point but acquires a finite width over a temperature range ΔT_c around the transition temperature T_c. In case of a second order phase transition, $\Delta T_c/T_c$ is approximately given by $\Delta T_c/T_c \sim 1/\sqrt{N}$ [30]. For typical nuclear sizes of N≈100, the influence of a second order phase transition may, therefore, be perceptible at temperatures deviating by as much as 10% from the critical value. Furthermore, for a classical van der Waals gas the latent heat increases close to the critical point with $\sqrt{1 - T/T_c}$ and reaches already at $T/T_c = 0.95$ values larger than $k_B T_c$. Thus, in finite systems typical features of a first-order phase transition - like a latent heat - and signals indicating the proximity of the critical point - like diverging moments - are not necessarily inconsistent, making the attempt to extract critical-point exponents - at least - a worthwhile and interesting venture.

11 Determination of Critical Parameters

The observation of a power law for the fragment mass distribution in proton induced reactions was interpreted as an indication of a critical phenomenon [18]. It was proposed to deduce critical parameters [23] and critical exponents [61]. This goal remained elusive, despite some early efforts [24, 62, 63], until the recent attempt of the Purdue group to determine the full set of critical exponents from exclusive fragmentation data [28, 29]. Even if one ignores the fact that a decaying fragment is a transient system, e.g. by minimizing dynamical effects [4, 64] by studying light-ion induced reactions or peripheral collisions in more symmetric systems, one still faces the questions of what are the unambiguous signatures of critical behavior and what are robust methods for the determination of critical parameters and exponents in small systems with only 100 - 200 constituents.

It has long been recognized that the apparent exponent τ_{eff} obtained by the fit of a power law $\sigma(Z) \propto Z^{-\tau_{\text{eff}}}$ to the fragment size distribution exhibits a minimum when plotted versus the temperature or the bombarding energy [24, 62, 65]. The Fisher droplet model [22] predicts for the concentration of clusters of size s the relation

$$n_s = q_0 \, s^{-\tau} \, X^{s^{\sigma}} Y^s \tag{5}$$

with two critical exponents τ and σ and the surface and volume terms

$$X = \exp\left(-\frac{\Delta F_s}{k_B T}\right) \qquad\qquad Y = \exp\left(-\frac{\Delta F_v}{k_B T}\right)$$

containing the surface and volume free energies F_s and F_v. This inspired the suggestion to associate the minimum value of τ_{eff} with the critical exponent τ and the position of the minimum with the experimental conditions leading to a second order phase transition [24].

A closer examination of the fragment size distribution given by Eq. (5), however, showed that the interplay between surface and volume terms leads to a minimum of τ_{eff} at temperatures substantially below the critical temperature [62]. The correct way to determine the critical temperature using the droplet model is therefore to fit the fragment size distribution with the full expression (5) and to search for the conditions leading to $X = Y = 1$. A fit with q_0, τ, σ, X and Y as free parameters is usually not feasible and in practice one or both exponents are fixed to the values of the liquid gas phase transition [62, 66].

A different way to reduce the number of fit parameters is to recognize that the surface tension vanishes at and above the critical temperature. This implies $X = 1$ and Eq. (5) reduces to the product of a power law and an exponential

$$n_s = q_0 \, s^{-\tau_1} \, \exp\left(\frac{s}{m_0}\right) \tag{6}$$

with three free parameters q_0, τ_1 and m_0. This functional form should describe the cluster size distribution on the 'gas side' and m_0 should tend to large values, effectively reducing (6) to a power law, when the critical point is approached.

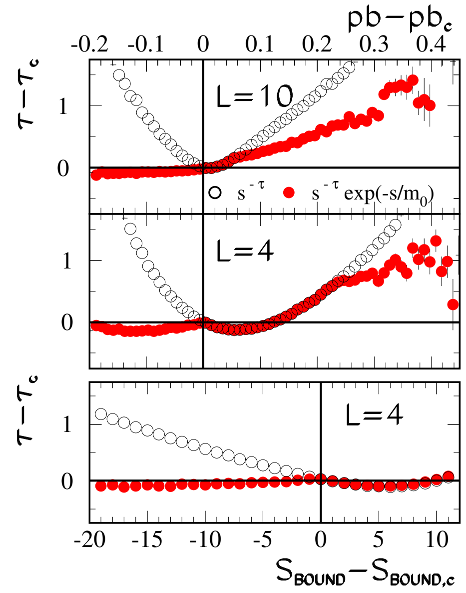

Figure 13: Percolation simulations: Deviation of the fitted τ values from the correct value $\tau_c = 2.18$ for fits with a pure power law (circles) and Eq. (6) (dots) versus the deviation of the control parameter from its critical value. L denotes the system size.

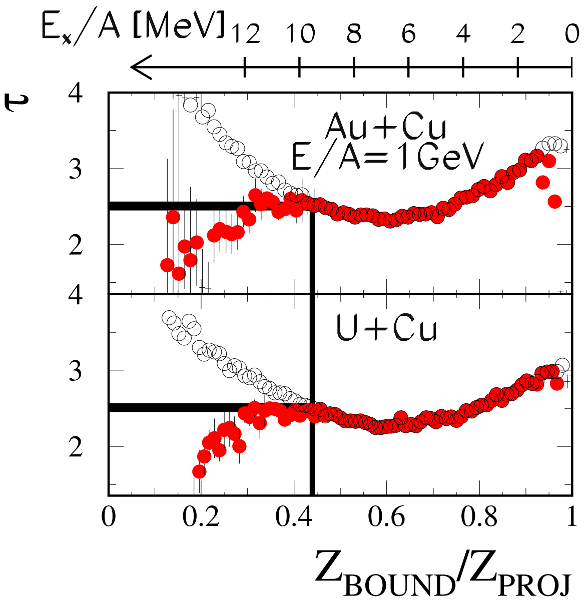

Figure 14: Experimental data: Apparent exponents τ versus reduced Z_{bound} for Au + Cu and U + Cu reactions at E/A = 1 GeV.

Following a proposal of Campi [61, 63], it has become customary to use percolation as a testing ground for analysis methods. Percolation on a large lattice exhibits many signatures of a second order phase transition [67], describes the formation of clusters and thus relates directly to observables of fragmentation experiments. Furthermore, calculations on small lattices show remarkable similarities to nuclear data [68, 7].

Cluster size distributions from a percolation simulation on a cubic lattice of length L were fitted in the range $2 \leq s \leq L^3/3$ with Eq. (6) and for comparison with a pure power law $n_s = q_0\, s^{-\tau_2}$. The relationship between the extracted τ values and the bond probability pb is shown in the upper part of Fig. 13. For small values of pb, in the 'gas phase', τ_1 is indeed close to the correct value $\tau_c = 2.18$ whereas τ_2 is substantially larger. When the critical region is approached τ_1 and τ_2 tend to the same value indicating that the cluster size distribution can now be described with a pure power law. Independent of the system size this transition takes place at the critical bond probability $pb_c = 0.249$ of the infinite lattice and exhibits a remarkably clear signature even for systems as small as $L = 4$.

Fragmentation reactions produce a broad distribution of system sizes and excitation energies. Therefore an estimate of the control parameter has to be determined event by event from the data itself. The potential distortions due to such a control parameter substitution were investigated by binning the percolation events according to $S_{bound} = \sum_{s\geq 2} s$, the analogue of the observable Z_{bound} used to characterize the energy deposition in nuclear collisions. The bottom part of Fig. 13 shows that even in this case one obtains an exponent close to the correct τ value and a critical S_{bound} which coincides with the average S_{bound} evaluated at the correct critical bond probability pb_c. The transition of the cluster size distribution shape to a pure power law is, therefore, a robust signature of the critical value of the control parameter in percolation.

The application of this method to projectile fragment distributions of Au and U induced reactions is demonstrated in Fig. 14. In both cases we find the transition at $Z_{bound}/Z_{proj} \approx 0.43$, corresponding to an excitation energy per nucleon of approximately 9-10 MeV, and a τ value of 2.5 ± 0.1. Caution should be exercised, however, when this result is interpreted in terms of a critical parameter, in this case the critical excitation energy. The relation between temperature and the excitation energy, shown on the cover page, exhibits a plateau - the temperature stays close to 5 MeV for excitation energies per nucleon between 3 and 10 MeV - suggestive of a phase transition of first order with a substantial latent heat. It is intriguing to see that the excitation energy associated with the transition to a pure power law coincides with the upper end of this plateau. Even though it is plausible that in a finite system some observables show signs of critical behavior while others exhibit features of a first order transition, it remains a challenging task for the future to develop a consistent picture - including effects of the long range Coulomb force and of the dynamical evolution of the system - and to extract quantitative estimates of phase transition parameters.

12 Summary

The available systematics reveal a universal behavior of multifragment decays of excited spectator nuclei for the range of bombarding energies $E/A = 400$ to 1000 MeV, and possibly to higher energies. This suggests that the mechanism of thermally driven decay remains the same and, furthermore, that the relation of excitation energy and mass for the produced spectators is virtually unchanged over this range of bombarding energies. In reactions with the lighter targets higher bombarding energies are needed in order to reach maximum fragment multiplicities and to achieve a complete disintegration of the projectile spectator. The corresponding lower limits are about 600 MeV and 1000 MeV per nucleon for the carbon and beryllium targets, respectively.

The momentum distributions of free neutrons measured with LAND are dominated by emission from a spectator source with approximately beam rapidity. Balance equations were used in order to determine the mass and excitation energy of the spectator system prior to its decay. The masses decrease and the excitation energies increase monotonously with decreasing Z_{bound}. The maximum excitation energies obtained from this analysis reach a value of 15 MeV per nucleon for the bin of smallest Z_{bound}.

A temperature scale was derived from observed yield ratios of He and Li isotopes. Rising first strongly with increasing excitation energy, the isotope temperature stays rather constant at a value of about 5 MeV for excitation energies between 3 and 10 MeV per nucleon. For higher excitation energies, again an increasing temperature is found. Depending on the low density equation-of-state the freeze-out in this vapor regime may by characterized by a density between 0.15 and 0.3 of normal nuclear density. The observed caloric curve agrees qualitatively with predictions of the Copenhagen multifragmentation model [36] and is reminiscent of the paradigm of a phase transition, the first-order phase transition of bulk (and also finite [46]) H_2O - systems.

J.P. and M.B. acknowledge the financial support of the Deutsche Forschungsgemeinschaft under the Contract No. Po256/2-1 and Be1634/1-1, respectively. This work was supported in part by the European Community under contract ERBCHGE-CT92-0003 and ERBCIPD-CT94-0091.

References

[1] M.B. Tsang *et al.*, Phys. Rev. Lett. **71**, 1502 (1993).

[2] W.C. Hsi *et al.*, Phys. Rev. Lett. **73**, 3367 (1994).

[3] W. Reisdorf *et al.*, Proceedings of the International Workshop XXII, Hirschegg, 1994, edited by H. Feldmeier and W. Nörenberg, p. 93;
S.C. Jeong *et al.*, Phys. Rev. Lett. **72**, 3468 (1994).

[4] G.J. Kunde *et al.*, Phys. Rev. Lett. **74**, 38 (1995).

[5] J. Bondorf *et al.*, Phys. Rev. Lett. **73**, 628 (1994).

[6] J. Hubele *et al.*, Z. Phys. A **340**, 263 (1991); Phys. Rev. C **46**, R1577 (1992).

[7] P. Kreutz *et al.*, Nucl. Phys. **A556**, 672 (1993).

[8] C.A. Ogilvie *et al.*, Phys. Rev. Lett. **67**, 1214 (1991).

[9] Th. Blaich *et al.*, Nucl. Instr. and Method **A314**, 136 (1992).

[10] S.B. Kaufman and E.P. Steinberg, Phys. Rev. C **22**, 167 (1980);
R.E.L. Green and R.G. Korteling, Phys. Rev. C **22**, 1594 (1980).

[11] P.L. Jain *et al.*, Phys. Rev. C **50**, 1085 (1994).

[12] X. Campi, H. Krivine, and E. Plagnol, Phys. Rev. C **50**, R2680 (1994).

[13] K. Sümmerer *et al.*, Phys. Rev. C **42**, 2546 (1990).

[14] A.S. Botvina *et al.*, Nucl. Phys. **A584**, 737 (1995).

[15] D.Q. Lamb *et al.*, Phys. Rev. Lett. **41**, 1623 (1978).

[16] H. Jaqaman, A.Z. Mekjian, and L. Zamick, Phys. Rev. C **27**, 2782 (1983) and Phys. Rev. C **29**, 2067 (1984).

[17] L. Satpathy, M. Mishra, and R. Nayak, Phys. Rev. C **39**, 162 (1989).

[18] J.E. Finn *et al.*, Phys. Rev. Lett. **49**, 1321 (1982).

[19] J. Kapusta, Phys. Rev. C **29**, 1735 (1984).

[20] A.L. Goodman, J. Kapusta, and A.Z. Mekjian, Phys. Rev C **30**, 851 (1984).

[21] D.H. Boal and A.L. Goodman, Phys. Rev. C **33**, 1690 (1986).

[22] M.E. Fisher, Physics **3**, 255 (1967).

[23] P.J. Siemens, Nature **305**, 410 (1983).

[24] A.D. Panagiotou *et al.*, Phys. Rev. Lett. **52**, 496 (1984); Phys. Rev. C **31**, 55 (19985).

[25] C.B. Chitwood *et al.*, Phys. Lett. **131B**, 289 (1983).

[26] J. Hüfner and D. Mukhopadhyay, Phys. Lett. B **173**, 373 (1986).

[27] R. Botet and M. Ploszajczak, Int. J. Mod. Phys. **E3**, 1033 (1994) and references therein.

[28] M.L. Gilkes *et al.*, Phys. Rev. Lett. **73**, 1590 (1994).

[29] J.B. Elliott *et al.*, Phys. Rev. C **49**, 3185 (1994).

[30] Y. Imry, Phys. Rev. B **21**, 2042 (1980).

[31] P. Labastie and R.L. Whetten, Phys. Rev. Lett. **65**, 1567 (1990).

[32] D.H. Boal and J.N. Glosli, Phys. Rev. C **42**, R502 (1990).

[33] Wang Neng-ping, Yang Shan-de, and Xu Gong-ou, J. Phys. G **20**, 101 (1994).

[34] G.T. Zheng, Phys. Rev C **50**, 771 (1994).

[35] S. Levit and P. Bonche, Nucl. Phys. **A437**, 426 (1985).

[36] J. Bondorf *et al.*, Nucl. Phys. A **444**, 460 (1985).

[37] D.H.E. Gross, Prog. Part. Nucl. Phys. **30**, 155 (1993).

[38] G. Bertsch and P.J. Siemens, Phys. Lett. **126B**, 9 (1983).

[39] J.A. Lopez and P.J. Siemens, Nucl. Phys. **A431**, 728 (1984).

[40] W.A. Friedman, Phys. Rev. C **42**, 667 (1990).

[41] M. Belkacem, V. Latora, and A. Bonasera, Phys. Lett. B **326**, 21 (1994).

[42] G. Papp and W. Nörenberg, Proceedings of the International Workshop XXII on Gross Properties of Nuclei and Nuclear Excitations, Hirschegg 1994, p. 87.

[43] G. Peilert *et al.*, Phys. Lett. B **260**, 271 (1991).

[44] H.-P. Cheng *et al.*, Phys. Rev. A **46**, 791 (1992).

[45] A. Hüller, Z. Phys. B **93**, 401 (1994).

[46] D.J. Wales and I. Ohmine, J. Chem. Phys. **98**, 7245 (1993).

[47] R. Blümel *et al.*, Nature **334**, 309 (1988).

[48] V. Lindenstruth, PhD thesis, University Frankfurt 1993, GSI-report GSI-93-18.

[49] S. Albergo *et al.*, Nuovo Cimento A **89**, 1 (1985).

[50] D. Hahn and H. Stöcker, Nucl. Phys. **A476**, 718 (1988).

[51] J. Konopka *et al.*, Phys. Rev. C **50**, 2085 (1994).

[52] R.J. Charity *et al.*, Nucl. Phys. **A483**, 371 (1988).

[53] R. Trockel *et al.*, Phys. Rev. C **39**, 729 (1989).

[54] R. Trockel, PhD thesis, University of Heidelberg 1988 (unpublished).

[55] C. Borcea *et al.*, Nucl. Phys. **A415**, 169 (1984).

[56] G. Nebbia *et al.*, Phys. Lett. B **176**, 20 (1986).

[57] D. Fabris *et al.*, Phys. Lett. B **196**, 429 (1987).

[58] G.J. Kunde *et al.*, Phys. Lett. B **272**, 202 (1991).

[59] W. Bohne *et al.*, Phys. Rev. C**41**, R5 (1990).

[60] W.A. Friedman, 8^{th} Winter Workshop on Nuclear Dynamics, Jackson Hole, Wyoming, January 1992.

[61] X. Campi, J. Phys. A **19**, L917 (1986).

[62] N. T. Porile *et al.*, Phys. Rev. **C 39**, 1914 (1989).

[63] X. Campi, Phys. Lett. **B 208**, 351 (1988).

[64] J. Pochodzalla *et al.*, Nucl. Phys. **A583**, 553c (1995).

[65] W. Trautmann *et al.*, Z. Phys. **A 344**, 447 (1993).

[66] V. Latora *et al.*, Phys. Rev. Lett. **73**, 1765 (1994).

[67] D. Stauffer and A. Aharony, *Introduction to Percolation Theory*, 2nd ed. (Taylor and Francis, London, 1992); D. Stauffer, Phys. Rep. **54**, 1 (1979).

[68] J. Desbois, Nucl. Phys. **A466**, 724 (1987).

W.F.J. Müller(1), J. Pochodzalla,(1) and W. Trautmann(1) for the ALADIN/LAND collaboration:

M. Begemann-Blaich,(1) Th. Blaich,(2) C. Groß,(1) H. Emling,(1) A. Ferrero,(3)* G. Immé,(4) I. Iori,(3) G.J. Kunde,(1)† W.D. Kunze,(1) V. Lindenstruth,(1)‡ U. Lynen,(1) T. Möhlenkamp,(5) A. Moroni,(3) B. Ocker,(6) G. Raciti,(4) T. Rubehn,(1) H. Sann,(1) A. Schüttauf,(6) C. Schwarz,(1) W. Seidel,(5) V. Serfling,(6) J. Stroth,(1) A. Trzcinski(7) A. Tucholski,(7) G. Verde,(4) A. Wörner,(1) E. Zude,(1) B. Zwieglinski(7)

(1)Gesellschaft für Schwerionenforschung, 64220 Darmstadt, Germany
(2)Institut für Kernchemie, Universität Mainz, 55099 Mainz, Germany
(3)Dipartimento di Fisica, Università di Milano and I.N.F.N., 20133 Milano, Italy
(4)Dipartimento di Fisica dell' Università and I.N.F.N., 95129 Catania, Italy
(5)Forschungszentrum Rossendorf, 01314 Dresden, Germany
(6)Institut für Kernphysik, Universität Frankfurt, 60486 Frankfurt, Germany
(7)Soltan Institute for Nuclear Studies, 00 681 Warsaw, Hoza 69, Poland

*On leave from the Comision Nacional Energia Atomica, Argentina
†Present address: National Superconducting Cyclotron Laboratory, Michigan State University, East Lansing, MI 48824, USA
‡Present address: Lawrence Berkeley Laboratory, Berkeley, CA 94720